CellPress

Trends in Biotechnology

Research Article

Optogenetic engineering of lipid droplet spatial organization for tumor suppression

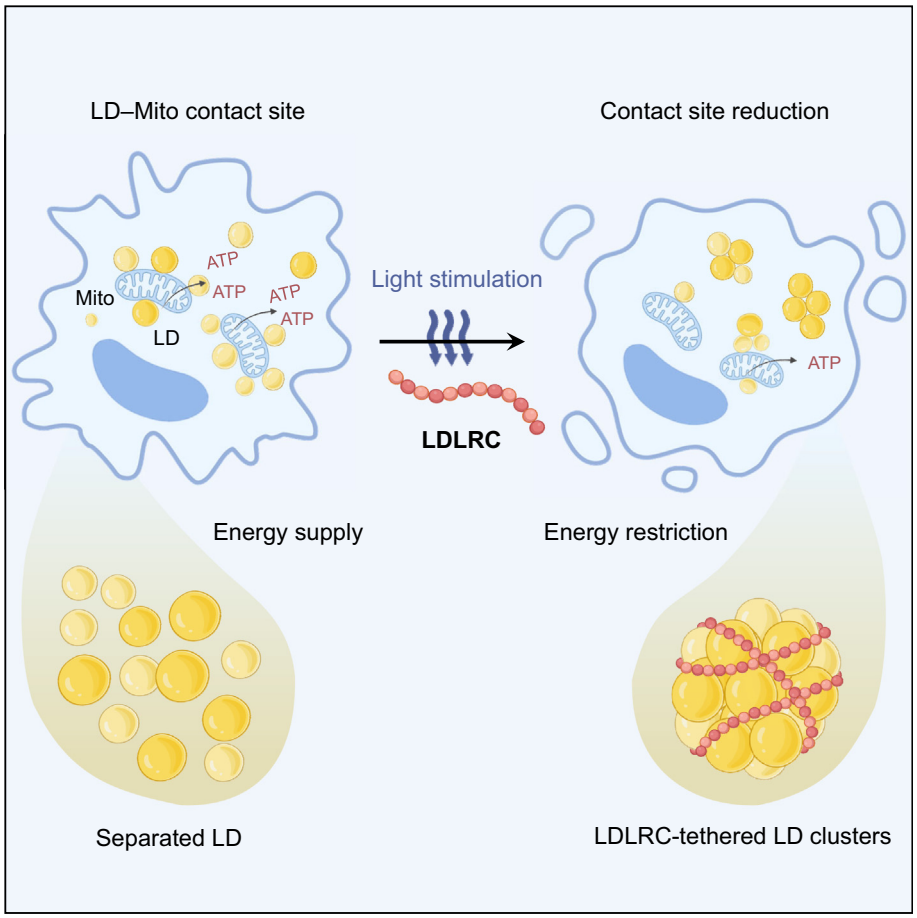

Optogenetic induction of lipid droplet clustering reduces fatty acid transfer during nutrient starvation, compromises energy production, and results in cancer cell death *in vitro* and tumor growth suppression *in vivo*. Our light-activated system for modulating lipid droplet dynamics presents a strategy to target cancer metabolism by interrupting organelle-mediated nutrient exchange.

Qingjie Bai (白清杰), Xintian Shao (邵新田), Qinghua Xia (夏庆华), Shuo Yang (杨硕), Yanan Gao (高雅楠), Kai Sun (孙恺), Jian Li (李建), Xiuxiu Wang (王秀秀), Zhiqi Tian (田芷淇), Xiaoyuan Chen (陈小元), Jing Zhao (赵劲), Jiajie Diao (刁佳杰), Qixin Chen (陈启鑫)

chen.shawn@nus.edu.sg (X. Chen), jingzhao@nju.edu.cn (J. Zhao), jiajie.diao@uc.edu (J. Diao) chenqixin@sdfmu.edu.cn (Q. Chen).

Highlights

Under nutrient stress, cancer cells exploit lipid droplets as an alternative energy reservoir, supporting mitochondrial functions through membrane contact sites.

The light-inducible lipid droplet clustering system reduces their accessibility for forming membrane contact sites with mitochondria.

Lipid droplet clustering reduces the energy supply to mitochondria by limiting the formation of membrane contact sites during cancer cell starvation.

Lipid droplet clustering suppresses tumor progression both *in vitro* and *in vivo*.

Trends in Biotechnology, November 2025, Vol. 43, No. 11
https://doi.org/10.1016/j.tibtech.2025.06.002

Trends in Biotechnology

CellPress

Research Article

Optogenetic engineering of lipid droplet spatial organization for tumor suppression

Qingjie Bai (白清杰)[1,2,11], Xintian Shao (邵新田)[2,3,11], Qinghua Xia (夏庆华)[2,11], Shuo Yang (杨硕)[2,11], Yanan Gao (高雅楠)[2], Kai Sun (孙恺)[2], Jian Li (李建)[2], Xiuxiu Wang (王秀秀)[4], Zhiqi Tian (田芷淇)[3], Xiaoyuan Chen (陈小元)[5,6,7,8,9,10,*], Jing Zhao (赵劲)[4,*], Jiajie Diao (刁佳杰)[3,*], and Qixin Chen (陈启鑫)[1,2,3,5,10,*]

In cancer cells, lipid droplets (LDs) establish extensive membrane contact sites (MCSs) with mitochondria to facilitate fatty acid transfer and sustain energy production, thus enabling cancer cell survival, in nutrient-deprived tumor microenvironments. However, effective strategies to disrupt these LD–mitochondria interactions remain unavailable. We engineered an optogenetic system to control LD intracellular organization through clustering. Upon blue light stimulation, the system induces LDs to undergo spatial reorganization and form clusters, thereby restricting LD accessibility by reducing the available surface area for mitochondrial interaction. Consequently, this clustering significantly diminishes the number of LD–mitochondria MCSs, suppresses fatty acid transport from LDs to mitochondria during starvation, and ultimately leads to cancer cell death *in vitro* and tumor growth inhibition *in vivo*. Collectively, our results demonstrate that optogenetically controlled LD clustering offers a novel approach to impede tumor progression by blocking nutrient flow from LDs to mitochondria.

Technology readiness

Our light-controlled responsive crosslinker (LDLRC)-based lipid droplet (LD) clustering regulation technology has currently reached Technology Readiness Level (TRL) 3, with proof of concept successfully demonstrated in controlled laboratory settings. To advance this technology to higher TRL stages, two critical challenges must be addressed: (i) optimizing tumor-specific expression of LDLRC and (ii) enhancing the penetration depth of blue light in biological tissues. Addressing these challenges will require targeted R&D efforts, including the refinement of *in vivo* gene-editing strategies and the development of safer, more efficient photoactivatable nanomaterials. At the policy level, the establishment of standardized frameworks for LDLRC-based LD clustering regulation is essential to ensure consistency, safety, and translational applicability in both research and clinical contexts.

Introduction

The rapid growth of solid tumors mainly leads to insufficient internal blood vessels, thereby creating a nutrient-deprived tumor microenvironment (TME) [1,2]. Despite these challenges, cancer cells continue to thrive in a nutrient-deprived TME by developing mechanisms that support robust growth and proliferation [3,4]. One such adaptation involves the use of lipid droplets (LDs) as reservoirs of energy and metabolic intermediates [5–7]. These LDs play a notable role in enabling tumor cells to thrive in nutrient-deprived environments [8], thereby contributing to their proliferation, survival, and ultimately cancer progression.

LDs are dynamic organelles that store neutral lipids, such as triglycerides and cholesterol esters, and regulate energy homeostasis, membrane synthesis, and lipid metabolism [9–11]. The formation of membrane contact sites (MCSs) between LDs and organelles is critical for essential cellular processes, such as autophagy and lipid metabolism [12–14]. In cancer cells, mitochondria play a crucial role in establishing these contacts with organelles such as LDs and lysosomes, which are the key to sustaining mitochondrial energy supply and supporting rapid cancer cell proliferation [15–18]. This is especially important for solid tumors that often grow in nutrient-deficient environments and then reprogram their metabolism away from glycolysis and toward fatty acid (FA) oxidation for ATP production [19–21]. To support these metabolic needs of tumor cells, mitochondria form extensive contacts with LDs to facilitate FA transport from these organelles that serve as the main cellular storage of neutral lipids [17,22]. Therefore, preventing contacts between LDs and mitochondria may represent a strategy to regulate tumor cell growth and inhibit tumor cell survival by blocking the flow of nutrients.

[1]School of Pharmacy, Naval Medical University (Second Military Medical University), Shanghai 200433, China
[2]School of Pharmaceutical Sciences, School of Life Sciences, Medical Science and Technology Innovation Center, Shandong First Medical University & Shandong Academy of Medical Sciences, Jinan, Shandong 250117, China
[3]Department of Cancer Biology, University of Cincinnati College of Medicine, Cincinnati, OH 45267, USA
[4]State Key Laboratory of Coordination Chemistry, Chemistry and Biomedicine Innovation Center (ChemBIC), ChemBioMed Interdisciplinary Research Center at Nanjing University, School of Chemistry and Chemical Engineering, Nanjing University, Nanjing, 210093, China

Meanwhile, the spatial arrangement of organelles can impact the formation of MCSs. For instance, the clustering of lysosomes on individual autophagosomes could form a prefusion status for multiple rounds of fusion [23]. Furthermore, several strategies for manipulating spatial distribution of mitochondria–lysosome contacts have been developed, including optogenetics tools and small-molecule dual-organelle targeting regulators [24–27]. Optogenetics has demonstrated remarkable potential in regulating organelle interactions and dynamics in recent years, leveraging its unique advantages of high spatiotemporal precision and reversibility [28,29]. Therefore, we could alter the MCSs by optogenetic control of the spatial arrangement of organelles.

Here, we engineered a light-controlled responsive crosslinker (LDLRC) for clustering LDs, which physically alters the spatial arrangement of LDs, thereby effectively reducing their accessible surface area and limiting the MCSs between LDs and mitochondria. As this light-controlled LD clustering restricts mitochondrial access to LD stores of FAs, particularly under nutrient-deficient conditions, we observed reduced energy metabolism and tumor growth both in cells and *in vivo*, which could offer a potential therapeutic opportunity across diverse cancer types.

Results

LDs support mitochondrial functions through MCSs

To investigate the role of LD–mitochondria interactions in cellular energy supply during nutrient-deprived conditions, we analyzed MCSs between these organelles in 786-O clear cell renal carcinoma cells. LDs were labeled with Lipi-Blue [30], and mitochondria were labeled with MitoTracker Deep Red [31] (Figure 1A). Following serum starvation, we observed a marked reduction in both the number and size of LDs (Figure 1B,C). However, the number of physical contacts between LDs and mitochondria significantly increased under these conditions (Figure 1D), accompanied by corresponding changes in mitochondrial morphology (Figure S1 in the supplemental information online). This phenomenon was consistently observed in other cancer cell lines, including HepG2 hepatocellular carcinoma cells and MCF-7 breast cancer cells (Figure S2 in the supplemental information online). Meanwhile, Seahorse metabolic flux analysis revealed a shift from glycolytic to mitochondrial respiration in serum-deprived cells, enabling the maintenance of overall energy production despite limited nutrients (Figure 1E and Figure S3 in the supplemental information online). Concurrently, measurements of mitochondrial FA β-oxidation (FAO) demonstrated enhanced FA metabolism-driven ATP production after nutrient deprivation (Figure 1F,G). These findings suggest that the increased number of LD–mitochondria contacts during serum starvation supports mitochondrial metabolic adaptation, specifically by promoting FA oxidation.

To assess the direct relationship between increased mitochondrial energy production and increased number of LD–mitochondria contacts during serum starvation, FA tracing experiments were conducted using the fluorescent FA probe C12 to monitor the fate of FAs released from the LDs [32,33] (Figure 1H,J). Under nutrient-deprived conditions, we detected a substantial release of FAs from LDs – indicated by reduced probe colocalization with LDs (Figure 1I) – and a concurrent increase in FA uptake by mitochondria, reflected by high colocalization with the mitochondrial marker (Figure 1K). These data imply that serum starvation promotes FA trafficking from LDs to mitochondria by increasing the LD–mitochondria contact (Figure 1L). Together, these observations support the hypothesis that LD–mitochondria contacts are critical for fueling mitochondrial energy metabolism under nutrient stress, and disrupting these contacts effectively diminishes energy production in cancer cells, ultimately hindering their survival.

Engineering light-inducible LD clustering system to reduce their accessibility

To test whether reducing LD–mitochondria interactions could attenuate mitochondrial energy metabolism, we reduced the accessibility of LDs by designing a system to cluster LDs, thereby

[5]Departments of Diagnostic Radiology, Surgery, Chemical and Biomolecular Engineering, and Biomedical Engineering, Yong Loo Lin School of Medicine and College of Design and Engineering, National University of Singapore, Singapore, 119074, Singapore
[6]Clinical Imaging Research Centre, Centre for Translational Medicine, Yong Loo Lin School of Medicine, National University of Singapore, Singapore 117599, Singapore
[7]Nanomedicine Translational Research Program, Yong Loo Lin School of Medicine, National University of Singapore, Singapore 117597, Singapore
[8]Theranostics Center of Excellence (TCE), Yong Loo Lin School of Medicine, National University of Singapore, 11 Biopolis Way, Helios, 138667, Singapore
[9]Institute of Molecular and Cell Biology, Agency for Science, Technology, and Research (A*STAR), 61 Biopolis Drive, Proteos, Singapore, 138673, Singapore
[10]Department of Pharmacy and Pharmaceutical Sciences, National University of Singapore, Lower Kent Ridge Road, 4 Science Drive 2, 117544, Singapore
[11]These authors contributed equally to this work

*Correspondence:
chen.shawn@nus.edu.sg (X. Chen), jingzhao@nju.edu.cn (J. Zhao), jiajie.diao@uc.edu (J. Diao), and chenqixin@sdfmu.edu.cn (Q. Chen).

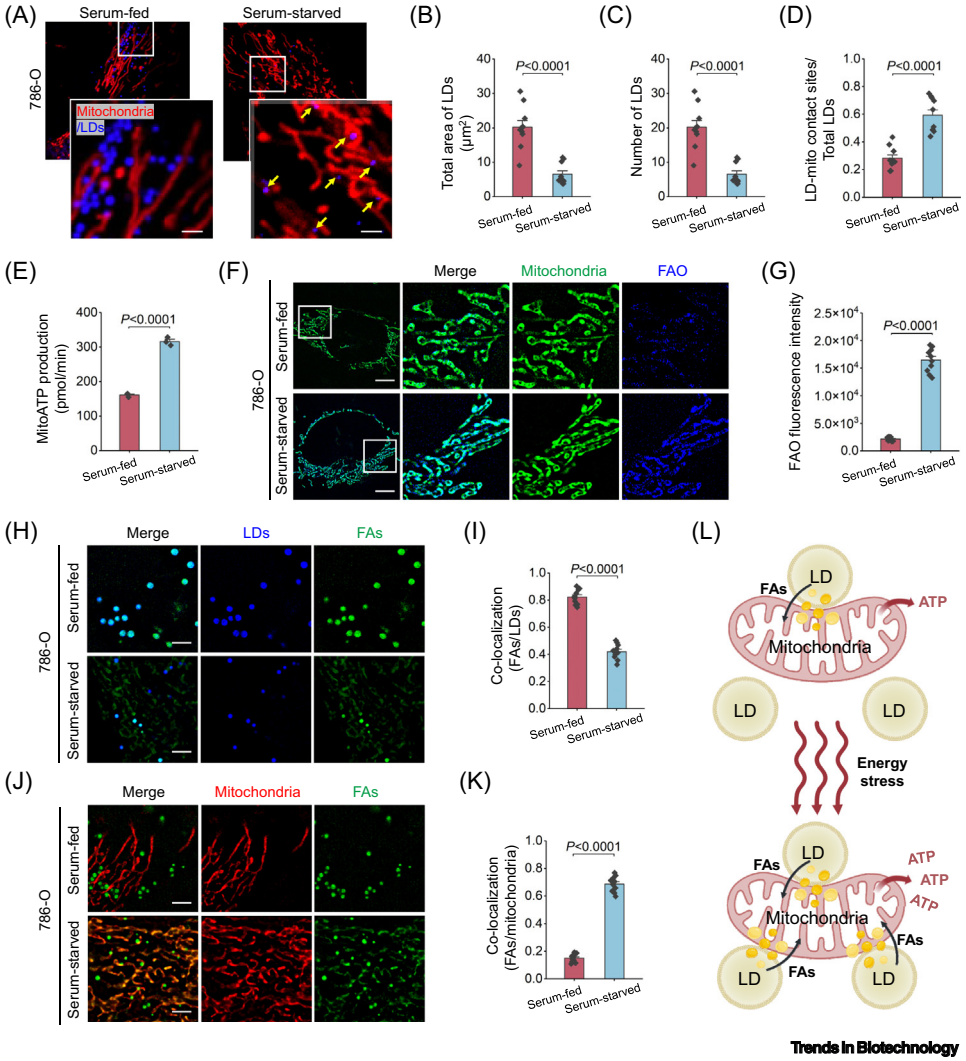

Figure 1. Lipid droplets (LDs) support mitochondrial function through membrane contact sites (MCSs). (A–D) Mitochondria labeled with MTDR and LDs labeled with Lipi-Blue in serum-fed and serum-starved 786-O cells. Yellow arrows indicate close contacts between LDs and mitochondria following serum starvation. (A) Representative images (scale bar, 2 μm). (B, C) Quantitative analysis of the total area and number of LDs (n = 10 cells). (D) Ratio of LD–mitochondria contacts (n = 10 cells). (E) Quantitative analysis of mitochondrial ATP production in serum-fed and serum-starved 786-O cells was conducted through Seahorse experiments (n = 3 measurements). (F, G) Fatty acid β-oxidation (FAO) probe labeling of mitochondrial FAO in serum-fed and serum-starved 786-O cells. (F) Representative super-resolution images (scale bar, 5 μm). (G) Quantitative analysis of FAO fluorescence intensity (n = 10 cells). (H, I) Tracking fatty acid (FA) distribution on LDs in 786-O cells under serum-fed and serum-starved conditions. (H) Representative super-resolution images (scale bar, 2 μm). (I) Quantitative analysis of FAs and LD colocalization (n = 10 cells). (J, K) Tracking FA distribution on mitochondria in 786-O cells under serum-fed and serum-starved conditions. (J) Representative super-resolution images (scale bar, 2 μm). (K) Quantitative analysis of FAs and mitochondrial colocalization (n = 10 cells). (L) Schematic representation of altered metabolic pathways in 786-O cells under serum-fed and serum-starved conditions. Created with BioRender.com. Statistical analysis was performed using a two-tailed unpaired Student's *t* test, and the data were presented as mean ± SEM. $P < 0.05$ was considered statistically significant.

reducing their accessible surface area for organelle contacts and blocking FA transport. This thus inhibits energy metabolism in nutrient-starved cancer cells. This system, termed LDLRC, leverages optogenetic control to induce LD clustering and limit their functional availability. The LDLRC construct comprises three components: protein Plin2 as the LD membrane anchor [34], a red

fluorescent protein mCherry for visualization, and the light-sensitive dimerization domain CRY2 [27,35–37] (Figure 2A). In the presence of blue light, CRY2 undergoes homodimerization, driving neighboring LDs closer and aggregation of adjacent LDs via Plin2-mediated anchoring. The LDLRC system was introduced into 786-O cells and successfully localized to LD membranes, as verified by costaining with Lipi-Blue for colocalization experiments (Figure 2B and Figure S4 in

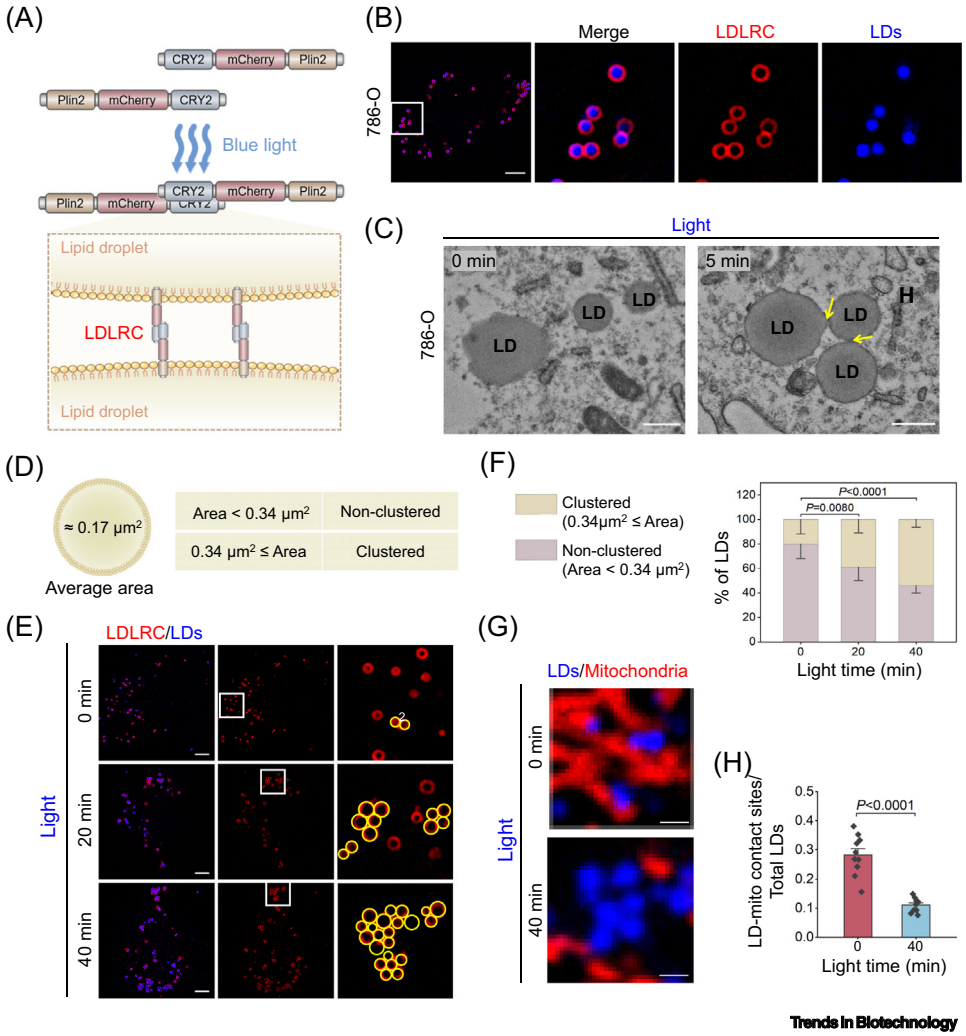

Figure 2. Engineering light-inducible stable lipid droplet (LD) clustering system to reduce accessibility. (A) Fusion of the light-sensitive protein CRY2 with the red fluorescent protein mCherry and the LD membrane protein Plin2 generates light-controlled responsive crosslinker (LDLRC), which leads to LD clustering upon illumination with the light. Created with BioRender.com. (B) Super-resolution imaging of LDLRC and the LD probe Lipi-Blue colocalized on LDs in 786-O cells (scale bar, 5 μm). (C) Transmission electron microscopy images of LDs in serum-starved 786-O cells under both nonlight and light-controlled conditions. Representative images (scale bar, 500 nm). (D) Evaluation criteria for the average area of LDs and whether LD clustering occurs in 786-O cells (n = 728 LDs from 20 cells). (E, F) Time-lapse imaging of LD clustering in LDLRC-expressing 786-O cells under light exposure. (E) Representative super-resolution images; yellow circles indicate clustered LDs (scale bar, 5 μm). (F) Quantitative analysis of LD clustering (n = 10 cells). (G, H) Changes in the LD–mitochondria contact ratio in LDLRC-expressing 786-O cells under light exposure versus no light exposure. (G) Representative images (scale bar, 1 μm). (H) Quantitative assessment of the LD–mitochondria contact ratio (n = 10 cells). Statistical analysis was performed using a two-tailed unpaired Student's *t* test, and the data were presented as mean ± SEM. $P < 0.05$ was considered statistically significant.

the supplemental information online). Comparable expression and localization were achieved in HepG2 and MCF-7 cells (Figure S5 in the supplemental information online).

Upon exposure to a custom-designed light source (500 μW/cm^2) [35] for durations of 0, 3, and 5 min, LDs were observed to progressively cluster (Figure S6A in the supplemental information online). This effect was confirmed through both transmission electron microscopy (Figure 2C) and live-cell imaging with alternative LD markers (Figures S6B,C in the supplemental information online). These results indicated that light-induced LDLRC promoted LD clustering. To quantify LD clustering, we analyzed 728 LDs and set an average LD area of 0.17 μm^2 as a baseline. LDs with areas <0.34 μm^2 were categorized as nonclustered, and those ≥0.34 μm^2 were classified as clustered (Figure 2D). Subsequently, quantitative analysis indicated that prolonged light exposure (20–40 min) significantly increased the proportion of clustered LDs (Figure 2E), accompanied by a reduction in nonclustered LDs (Figure 2F). Importantly, light-induced LD clustering led to a substantial reduction in LD–mitochondria contact (Figure 2G,H), indicating effective spatial segregation. These effects were CRY2-dependent because cells expressing a control version of LDLRC lacking CRY2 (LDLRC-c) exhibited no LD clustering under light stimulation (Figure S7 in the supplemental information online). Moreover, the LDLRC system consistently induced LD clustering in HepG2 and MCF-7 cells (Figure S8 in the supplemental information online).

To assess the stability of LDLRC-tethered LD clusters, we terminated light exposure and monitored cells over an 8-h period. LD clusters persisted in the absence of light (Figure S9 in the supplemental information online), suggesting that CRY2-mediated tethering may trigger endogenous stabilization mechanisms. It was found that the tethered LDs did not disperse, suggesting that LDLRC-tethering can further initiate endogenous LD tethering factors such as Cidec (Figure S10 in the supplemental information online). Collectively, our data demonstrate that LDLRC enables light-inducible control over LD clustering in cancer cells, resulting in stable LD clusters and a reduction in LD accessibility, ultimately reducing the formation of LD–mitochondria MCSs.

LD clustering decreases the energy supply during cancer cell starvation

To investigate the functional consequences of LD clustering during metabolic stress, we subjected the cells to serum-free starvation for 2 h to activate intracellular lipid use (Figure S11). Under these conditions, light-induced LD clustering (Figure 3A,B; 40-min exposure) inhibited lipid catabolism, as evidenced by a significantly enlarged area of Lipi-Blue–labeled LDs compared with nonirradiated controls (Figure 3C). These results suggest that clustered LDs are less accessible and less metabolically active than dispersed LDs. To support this, we next assessed the impact of nonclustered and clustered LDs on mitochondrial energy metabolism (Figure 3D–G). LD clustering was associated with a marked reduction in LD–mitochondria contact sites (Figure 3E), accompanied by decreased mitochondrial ATP production and oxygen consumption rate (Figure 3F,G and Figure S12 in the supplemental information online). These data indicate that clustered LD limits the transfer of metabolic substrates to mitochondria by obstructing MCSs between LD and mitochondria. To further substantiate this, we monitored FA transfer between LDs and mitochondria under starvation conditions. FA transfer was significantly suppressed in LDLRC-induced LD clusters (Figure 3H,J), mirroring the effects of etomoxir, an FA transport inhibitor. In LDLRC-induced clusters, FAs remained trapped in LDs (indicated by a high colocalization with LDs; Figure 3I) and were largely absent from mitochondria (demonstrated by a low colocalization with mitochondria; Figure 3K). By contrast, in nutrient-rich conditions where glycolysis and not mitochondrial FA metabolism dominates energy production, LDLRC-mediated LD clustering had no significant impact on ATP production (Figure S13 in the supplemental information online). Collectively, these findings suggest that LDLRC-mediated LD clustering effectively disrupts mitochondrial FA oxidation under starvation, exacerbating energy deprivation in cancer cells (Figure 3L).

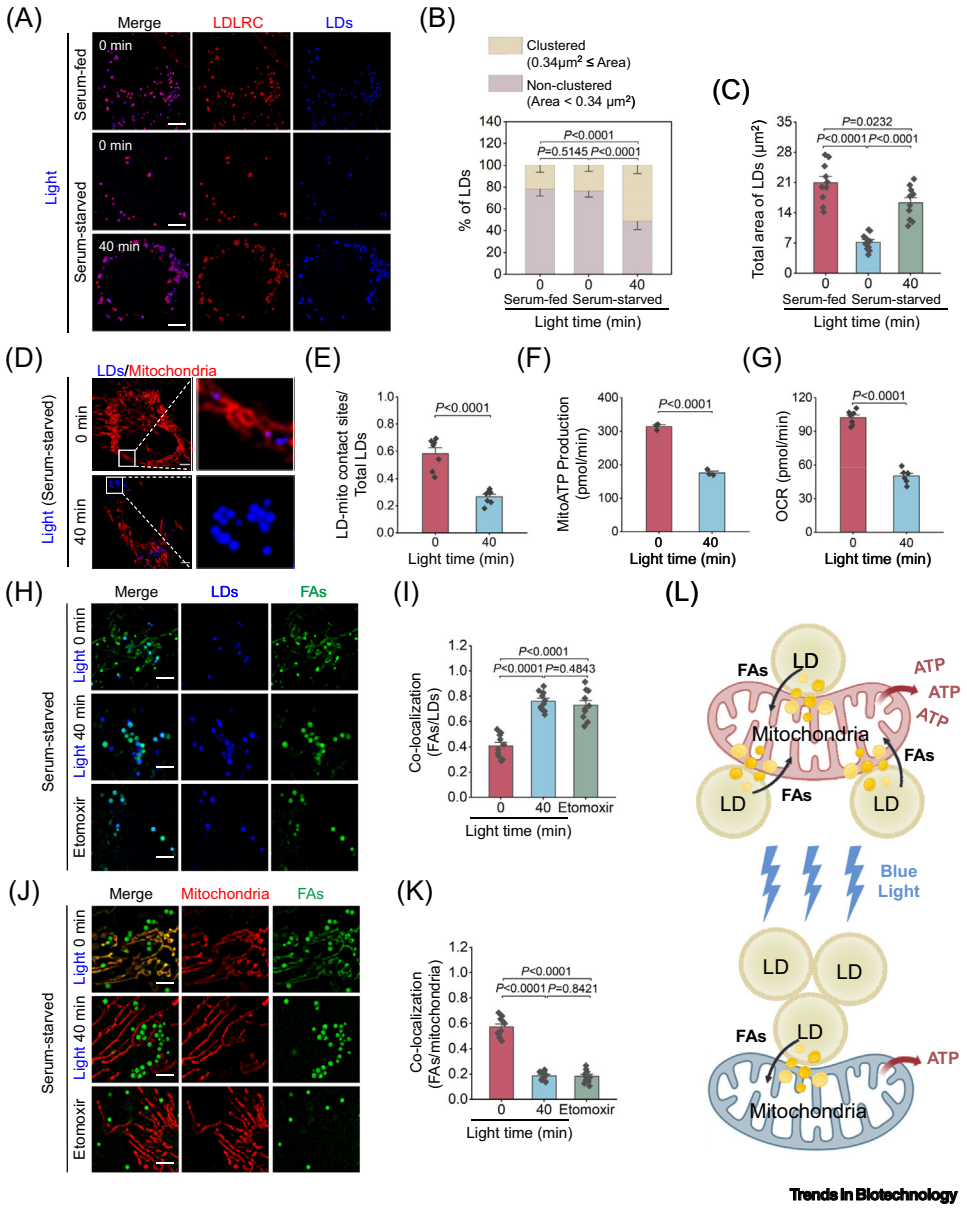

Figure 3. Lipid droplet (LD) clustering decreases the energy supply during cancer cell starvation. (A–C) Changes in LDs in LDLRC-expressing 786-O cells under serum-fed/no light exposure, serum-starved/no light exposure, and serum-starved/light exposure conditions. (A) Representative super-resolution images (scale bar, 5 μm). (B) Quantitative analysis of LD clustering (n = 7 cells). (C) Quantitative analysis of LD area (n = 7 measurements). (D, E) Evaluation of LD–mitochondria contact in serum-starved 786-O cells under nonlight and light-controlled conditions. (D) Representative images (scale bar, 5 μm). (E) Quantitative assessment of the LD–mitochondria contact ratio (n = 7 cells). (F, G) Quantitative analysis of the mitochondrial ATP production (n = 3 measurements) and oxygen consumption rate (OCR) (n = 7 measurements) in serum-starved 786-O cells under nonlight and light-controlled conditions. (H, I) Colocalization of fatty acids (FAs) with LDs in serum-starved 786-O cells under nonexposure, exposure, and etomoxir-treated conditions. (H) Representative super-resolution images (scale bar, 2 μm). (I) Quantitative analysis of FAs and LD colocalization (n = 10 cells). (J, K) Colocalization of FAs with mitochondria in serum-starved 786-O cells under nonexposure, exposure, and etomoxir-treated conditions. (J) Representative super-resolution images (scale bar, 2 μm). (K) Quantitative analysis of FAs and mitochondrial colocalization (n = 10 cells). (L) Schematic diagram of impaired LD use in serum-starved 786-O cells following light-induced control of LD clustering. Created with BioRender.com. Statistical analysis was performed using a two-tailed unpaired Student's *t* test, and the data were presented as mean ± SEM. $P < 0.05$ was considered statistically significant.

LD clustering suppresses tumor progression both *in vitro* and *in vivo*

To evaluate the therapeutic potential of LDLRC-mediated LD clustering, we conducted *in vitro* and *in vivo* studies. Flow cytometric analysis revealed a light dose-dependent progressive increase in late apoptosis, excluding phototoxicity in control groups (Figure S14 in the supplemental information online). Scratch assays confirmed that LDLRC treatment significantly impaired cell migration under starvation for over 12 h (mitomycin C–treated to suppress proliferation) (Figure 4A,B), whereas proliferation assays demonstrated suppressed growth of 786-O cells following light-induced LD clustering across various durations of serum deprivation (Figure 4C,D). To mimic nutrient-limited TMEs [38], we used tumor spheroid models. LDLRC expression and subsequent light activation significantly impeded spheroid expansion compared with controls (Figure 4E,F), confirming the antitumor potential of LD clustering under physiologically relevant conditions.

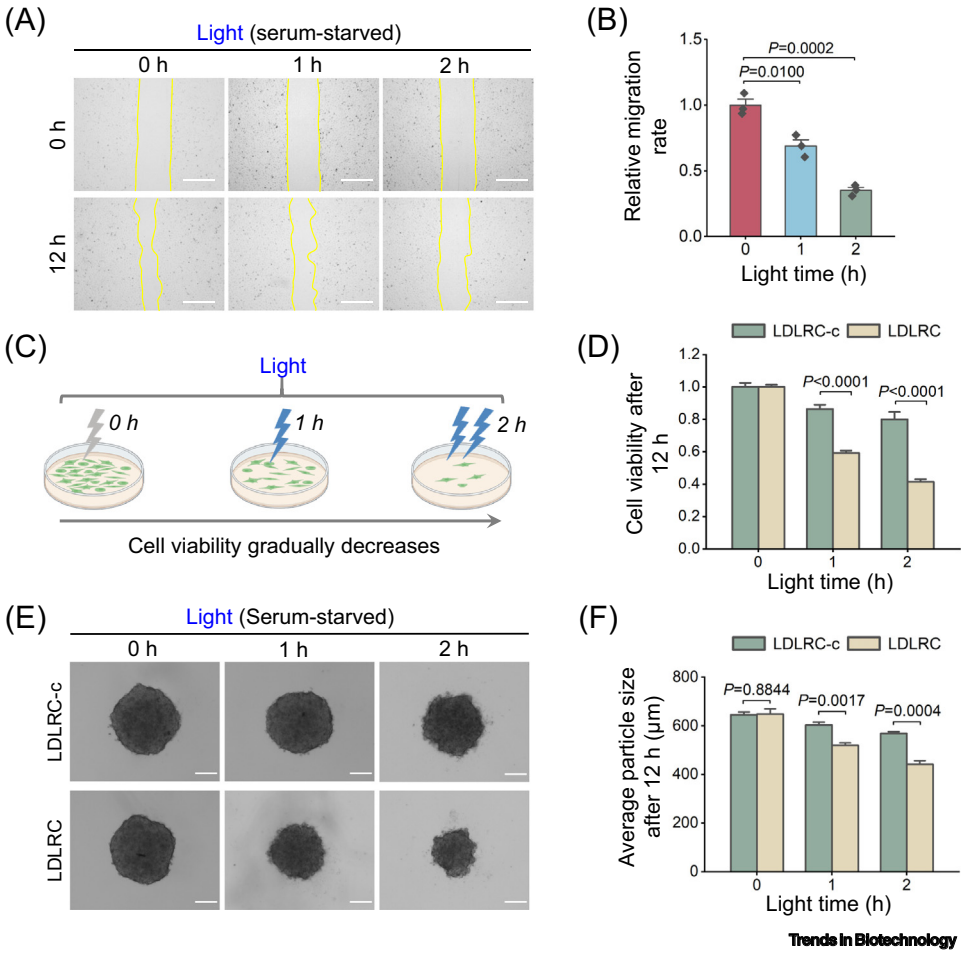

Figure 4. Lipid droplet (LD) clustering suppresses tumor progression *in vitro*. (A, B) Migration of serum-starved 786-O cells (mitomycin C–treated) in scratch wound assays at 12 h under different light exposure durations (0, 1, 2 h). (A) Representative images (scale bar, 500 μm). (B) Quantitative analysis of cell migration rate (n = 3). (C, D) Proliferation status of serum-starved 786-O cells at different light exposure durations (0, 1, 2 h) after 12 h. (C) Diagram illustrating a decrease in cell viability rate. Created with BioRender.com. (D) Quantitative analysis of cell viability rate (n = 4). (E, F) Growth status of serum-starved 786-O cell spheroids at different light exposure durations (0, 1, 2 h) after 12 h. (E) Representative images (scale bar, 200 μm). (F) Quantitative analysis of cell spheroid diameter (n = 3). Statistical analysis was performed using a two-tailed unpaired Student's *t* test, and the data were presented as mean ± SEM. $P < 0.05$ was considered statistically significant.

Given the limited tissue penetration of blue light, we employed upconverting nanoparticles (UCNPs) [39] to convert near-IR (NIR) light, displaying significantly greater tissue penetration, into blue light for *in vivo* activation of LDLRC within the tumor (Figure 5A). NIR light applied through the skin of tumor-bearing mice successfully triggered blue light emission from intratumoral UCNPs, subsequently activating the LDLRC system and promoting significant LD clustering and fusion (Figure 5B and Figure S15 in the supplemental information online). Once tumor volume (786-O cells) reached approximately 100 mm^3, 150 μg UCNPs were uniformly injected intratumorally, as

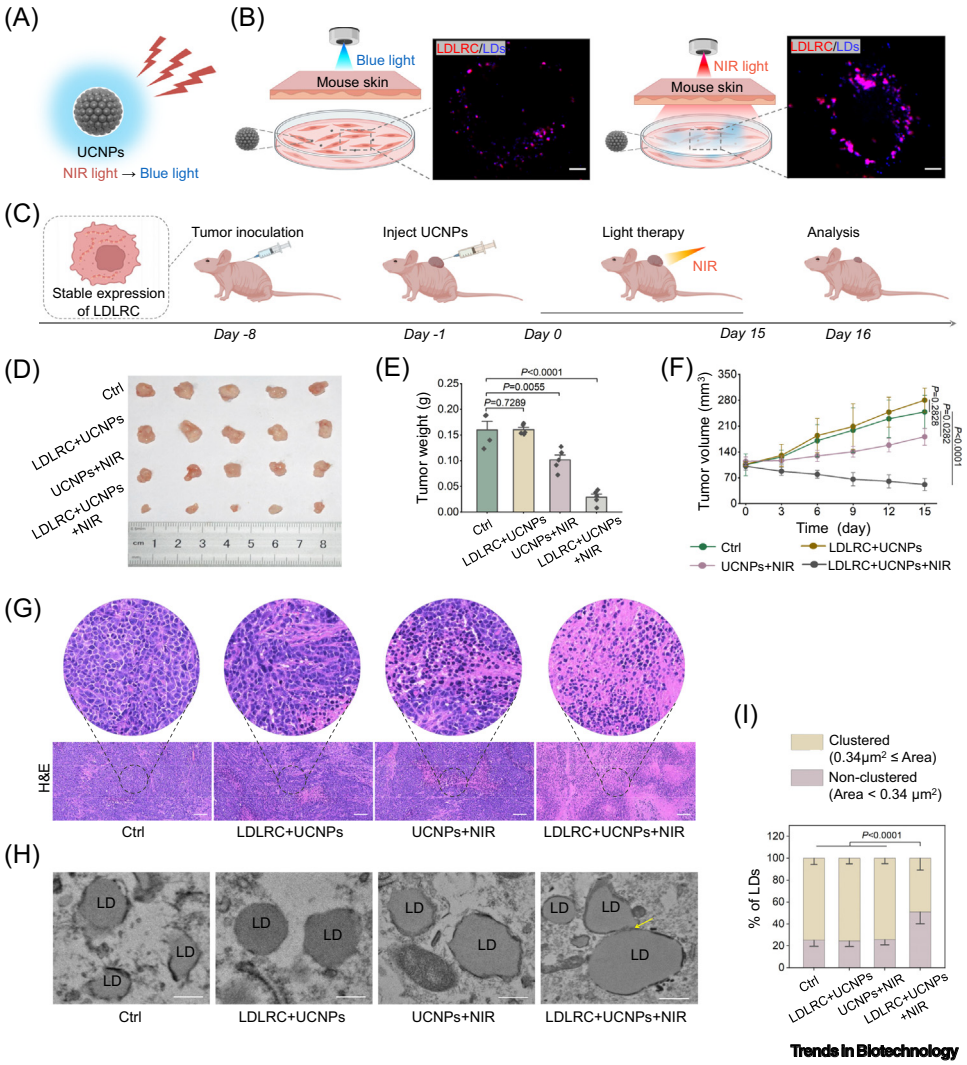

Figure 5. Lipid droplet (LD) clustering suppresses tumor progression *in vivo*. (A) Schematic diagram illustrating the conversion of near-IR (NIR) light to blue light by nanomaterial upconverting nanoparticles (UCNPs). Created with BioRender.com. (B) Blue light and NIR light exposure of 786-O cells expressing LDLRC through mouse skin. Representative images (scale bar, 5 μm). Created with BioRender.com. (C) Timeline of the animal experiments. Created with BioRender.com. (D) Images of tumors dissected from different groups of mice (n = 5). (E) Comparison of tumor weight following dissection among different groups of mice (n = 5). (F) Trends in tumor volume growth among different groups of mice (n = 5). (G) Images of tumor tissue sections from four groups stained with H&E. Representative images (scale bar, 200 μm). (H, I) Transmission electron microscopy images of tumor tissues from the four groups. (H) Representative images (scale bar, 200 nm). (I) Quantitative analysis of LD clustering (n = 10 cells). Statistical analysis was performed using a two-tailed unpaired Student's *t* test, and the data were presented as mean ± SEM. $P < 0.05$ was considered statistically significant.

reported in the relevant literature [39,40], followed by daily NIR light exposure (2 W/cm^2) [39,41] (Figure 5C). After 15 days of NIR treatment, LDLRC-expressing tumors exhibited significantly reduced growth (Figures 5D), weight (Figure 5E), and volume (Figure 5F and Figure S16 in the supplemental information online), compared with controls, without affecting overall body weight (Figure S17 in the supplemental information online). Moreover, H&E staining revealed significantly reduced tumor cell proliferation (Figure 5G) and prominent LD clustering (Figure 5H,I). Overall, our results validate that LDLRC, in combination with UCNPs, enables effective light-controlled LD clustering and exerts potent antitumor effects.

Discussion

In this study, we engineered an LDLRC system composed of the LD membrane-associated protein Plin2 [34], a red fluorescent marker mCherry, and the light-responsive optogenetic protein

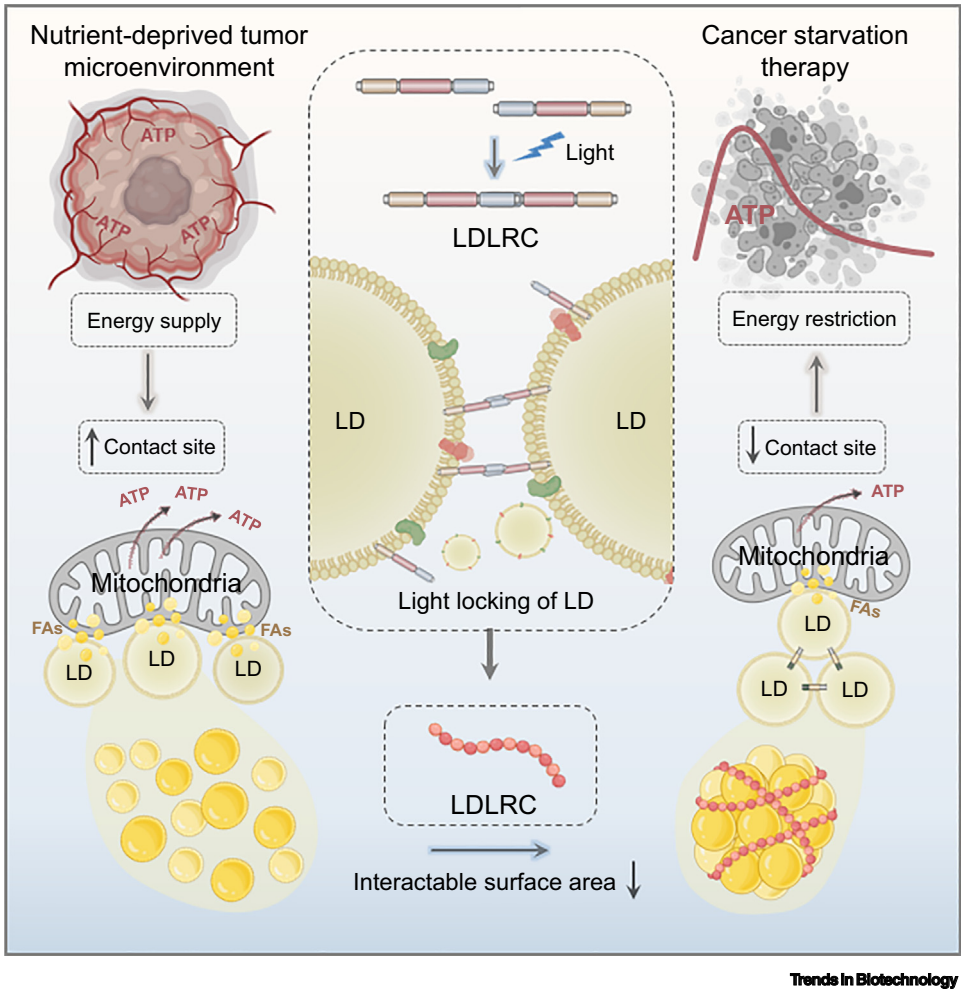

Figure 6. Schematic illustration of engineering light-inducible lipid droplet (LD) clusters for tumor suppression. Cancer cells respond to energy stress in nutrient-deprived tumor microenvironment (TME) by enhancing the contact between LDs and mitochondria. This study used a light-controlled responsive crosslinker (LDLRC) to induce clustering of LDs under blue light. By expressing LDLRC on the LD surface, close bundling of LDs was achieved, significantly reducing the interactable surface area of LDs, thereby effectively limiting their contact with mitochondria. This disruption of LD–mitochondria contact could prevent cancer cells from using LDs to mitigate energy stress.

CRY2 [27,35,36]. LDLRC-driven LD clustering reduces LD accessibility by decreasing the size of the interactable surface area and thus limiting the interaction of LDs with mitochondria. This spatial reorganization of LDs disrupts the transfer of FAs from LDs to mitochondria, especially under nutrient-deprived conditions where FA oxidation becomes essential for survival. Consequently, LD clustering impairs mitochondrial ATP production, sensitizes cancer cells to starvation, and suppresses tumor growth *in vitro* and *in vivo* (Figure 6). Overall, these studies suggest that blocking LD–mitochondria interactions may offer a promising therapeutic strategy for solid tumors within hypoxic and nutrient-deprived TMEs.

Compared with the conventional molecular approaches for modulating LD–mitochondria contacts [17,32,33,42], the engineered LDLRC system offers several advantages [43–45]. First, LDLRC does not directly act on the LD–mitochondrial MCS but restricts this contact by reducing the LD's interactable surface area, effectively avoiding uncertain interference factors. Second, the LDLRC-mediated regulation of LD–mitochondria contact was highly specific, because LD–mitochondria contact was restricted to only sites expressing LDLRC components and receiving light exposure. Finally, LD–mitochondria contact restriction is remarkably rapid, which initiates the limiting effect immediately after light exposure.

Despite the promising outcomes of the LDLRC system, several challenges must be addressed for its effective *in vivo* application. A primary limitation is the poor tissue penetration of blue light, which constrains its therapeutic efficacy in deep-seated tissues. To overcome this, UCNPs have been developed to convert NIR light – known for superior tissue penetration, into localized blue light at the target site [40,46]. Another major challenge is achieving cell-specific expression of optogenetic components (e.g., LDLRC) within living organisms. Encouragingly, recent developments in CRISPR-Cas9 delivery systems have demonstrated the feasibility of cell subtype-specific gene editing *in vivo* [47], offering new avenues for precise optogenetic modulation.

Furthermore, compared with conventional cancer starvation therapies, which primarily aim to inhibit tumor vasculature and restrict the intake of nutrients (e.g., glucose and amino acids) [48,49], our approach addresses the challenge of metabolic plasticity by targeting alternative nutrient reservoirs that hinder effective treatment. Furthermore, given the crucial role of LDs in serving as an alternative nutrient reservoir in cancer cells and being implicated in lipid storage- and mobilization-associated disorders (e.g., obesity, diabetes, and nonalcoholic fatty liver disease) [50–54], LDLRC-mediated LD clustering may offer broader therapeutic potential beyond oncology.

Concluding remarks

In this study, we discovered that cancer cell mitochondria use LDs through LD–mitochondria interactions to compensate for energy deficits under starvation conditions. On the basis of this finding, we developed an LDLRC to precisely regulate LD–mitochondria interactions in cancer cells. By specifically targeting LDLRC to LD membranes, we achieved spatiotemporal control over LD clustering in cancer cells. This approach effectively inhibited starved cancer cells from accessing their nutrient reservoir via LD–mitochondria interactions, without directly perturbing LD–mitochondria MCSs. The blockade of this critical nutrient reservoir significantly impaired cancer cell survival and progression in nutrient-deprived tumor microenvironments. In summary, LDLRC not only effectively intervenes in LD–mitochondria interactions but also represents a novel organelle manipulation strategy that avoids direct interference with membrane contact sites. This strategy can be potentially extended to the broader field of organelle interaction research, providing a powerful tool for investigating interorganelle communication. Moreover, our work demonstrates a tumor starvation therapy targeting lipid metabolism (see Outstanding questions), overcoming the

Outstanding questions

To achieve specific expression of LDLRC on lipid droplets in various cancer cell types while minimizing effects on adjacent normal tissues, what strategies can be employed to selectively target LDLRC to lipid droplets in cancer cells?

Given that *in vivo* tumors are typically located deep within tissues and blue light has limited penetration depth, is it possible to enhance blue light penetration or develop materials that can emit blue light specifically at the tumor site?

Given that high-intensity or prolonged blue light exposure can cause phototoxicity, is it feasible to develop an LDLRC system that can be activated by near-IR light, which is associated with lower phototoxicity?

limitations of conventional starvation therapies and significantly advancing their therapeutic efficacy and clinical potential.

STAR★METHODS

Detailed methods are provided in the online version of this paper and include the following:

- KEY RESOURCES TABLE
- EXPERIMENTAL MODEL AND SUBJECT DETAILS
  - Cell culture
  - Animals
- METHOD DETAILS
  - Engineering LDLRC expression and cell staining
  - Live-cell imaging
  - ATP quantitative analysis and OCR measurement
  - FA migration detection
  - Quantification of LD clustering
  - Light source construction
  - Cell scratch and proliferation assay
  - Efficacy assessment at the cellular spheroid level
  - Lentiviral transfection and resistance screening
- QUANTIFICATION AND STATISTICAL ANALYSIS

RESOURCE AVAILABILITY

Lead contact

Further information and requests for resources and reagents should be directed to and will be fulfilled by the lead contact, Dr. Jiajie Diao (jiajie.diao@uc.edu).

Materials availability

The unique materials generated in this study can be obtained from the lead contact upon request.

Data and code availability

All data reported in this paper will be shared by the lead contact upon request. This paper does not report original code. Any additional information required to reanalyze the data reported in this paper is available from the lead contact upon request.

Acknowledgments

Q.C. was funded by Young Elite Scientists Sponsorship Program by CACM (CACM-2023-QNRC1-02), Shandong Province Key R&D Program (Major Technological Innovation Project) (2021CXGC010501), National Natural Science Foundation of China (No. 22107059), Natural Science Foundation of Shandong Province (ZR2021QH057), Innovation Team of Shandong Higher School Youth Innovation Technology Program (2021KJ035), Taishan Scholars Program (TSQN202211221), Shandong Science Fund for Excellent Young Scholars (ZR2022YQ66), and Joint Innovation Team for Clinical & Basic Research (202408); J.Z. was supported by National Natural Science Foundation of China (No. 22025701); X.C. was supported by National University of Singapore (NUHSRO/2020/133/Startup/08, NUHSRO/2023/008/NUSMed/TCE/LOA, NUHSRO/2021/034/TRP/09/Nanomedicine, 23-0173-A0001), National Medical Research Council (MOH-001388-00, CG21APR1005, MOH-001500-00, MOH-001609-00), Singapore Ministry of Education (MOE-000387-00, MOET32023-0005), and National Research Foundation (NRF-000352-00).

Author contributions

Q.B., X.C., J.Z., J.D., and Q.C. designed research; Q.B., X.S., Q.X., S.Y., Y.G., K.S., J.L., and X.W. performed research; Q.B., X.S., and Q.X. analyzed data; Q.B., Z.T., X.C., J.Z., J.D., and Q.C. wrote the paper.

Declaration of interests

The authors declare no competing financial interests.

Supplemental information

Supplemental information associated with this article can be found online at https://doi.org/10.1016/j.tibtech.2025.06.002.

References

1. de Visser, K.E. and Joyce, J.A. (2023) The evolving tumor microenvironment: from cancer initiation to metastatic outgrowth. *Cancer Cell* 41, 374–403
2. Pan, M. *et al.* (2022) Glutamine deficiency in solid tumor cells confers resistance to ribosomal RNA synthesis inhibitors. *Nat. Commun.* 13, 3706
3. Barba, I. *et al.* (2024) Targeting the Warburg effect in cancer: where do we stand? *Int. J. Mol. Sci.* 25, 3142
4. Wang, Y. and Patti, G.J. (2023) The Warburg effect: a signature of mitochondrial overload. *Trends Cell Biol.* 33, 1014–1020
5. Koundouros, N. and Poulogiannis, G. (2020) Reprogramming of fatty acid metabolism in cancer. *Br. J. Cancer* 122, 4–22
6. Jarc, E. and Petan, T. (2019) Lipid droplets and the management of cellular stress. *Yale J. Biol. Med.* 92, 435–452
7. Luo, W. *et al.* (2022) Adding fuel to the fire: the lipid droplet and its associated proteins in cancer progression. *Int. J. Biol. Sci.* 18, 6020–6034
8. Liu, R. *et al.* (2021) Choline kinase alpha 2 acts as a protein kinase to promote lipolysis of lipid droplets. *Mol. Cell* 81, 2722–2735.e9
9. Zadoorian, A. *et al.* (2023) Lipid droplet biogenesis and functions in health and disease. *Nat. Rev. Endocrinol.* 19, 443–459
10. Mathiowetz, A.J. and Olzmann, J.A. (2024) Lipid droplets and cellular lipid flux. *Nat. Cell Biol.* 26, 331–345
11. Chen, R. *et al.* (2022) Rational design of novel lipophilic aggregation-induced emission probes for revealing the dynamics of lipid droplets during lipophagy and ferroptosis. *Anal. Chem.* 94, 13432–13439
12. Prinz, W.A. *et al.* (2020) The functional universe of membrane contact sites. *Nat. Rev. Mol. Cell Biol.* 21, 7–24
13. Voeltz, G.K. *et al.* (2024) Making the connection: how membrane contact sites have changed our view of organelle biology. *Cell* 187, 257–270
14. Ye, Z. *et al.* (2023) Burst of hopping trafficking correlated reversible dynamic interactions between lipid droplets and mitochondria under starvation. *Exploration (Beijing)* 3, 20230002
15. Miller, D.R. and Thorburn, A. (2021) Autophagy and organelle homeostasis in cancer. *Dev. Cell* 56, 906–918
16. Wu, H. *et al.* (2023) Novel tumor therapy strategies targeting endoplasmic reticulum-mitochondria signal pathways. *Ageing Res. Rev.* 88, 101951
17. Meng, Y. *et al.* (2024) Glycolytic enzyme PFKL governs lipolysis by promoting lipid droplet-mitochondria tethering to enhance beta-oxidation and tumor cell proliferation. *Nat. Metab.* 6, 1092–1107
18. Berardi, D.E. *et al.* (2022) Lipid droplet turnover at the lysosome inhibits growth of hepatocellular carcinoma in a BNIP3-dependent manner. *Sci. Adv.* 8, eabo2510
19. Bian, X. *et al.* (2021) Lipid metabolism and cancer. *J. Exp. Med.* 218, e20201606
20. Martin-Perez, M. *et al.* (2022) The role of lipids in cancer progression and metastasis. *Cell Metab.* 34, 1675–1699
21. Vogel, F. *et al.* (2024) Lipids as mediators of cancer progression and metastasis. *Nat. Can.* 5, 16–29
22. Ye, Z. *et al.* (2019) Mitochondrion-specific blinking fluorescent bioprobe for nanoscopic monitoring of mitophagy. *ACS Nano* 13, 11593–11602
23. Chen, Q. *et al.* (2021) Prefused lysosomes cluster on autophagosomes regulated by VAMP8. *Cell Death Dis.* 12, 939
24. Zhang, C. *et al.* (2021) Long-term live-cell lipid droplet-targeted biosensor development for nanoscopic tracking of lipid droplet-mitochondria contact sites. *Theranostics* 11, 7767–7778
25. Qiu, K. *et al.* (2022) Light-activated mitochondrial fission through optogenetic control of mitochondria-lysosome contacts. *Nat. Commun.* 13, 4303
26. Ye, H. *et al.* (2011) A synthetic optogenetic transcription device enhances blood-glucose homeostasis in mice. *Science* 332, 1565–1568
27. Gautier, A. *et al.* (2014) How to control proteins with light in living systems. *Nat. Chem. Biol.* 10, 533–541
28. Duan, L. *et al.* (2015) Optogenetic control of molecular motors and organelle distributions in cells. *Chem. Biol.* 22, 671–682
29. Song, Y. *et al.* (2022) Light-inducible deformation of mitochondria in live cells. *Cell Chem. Biol.* 29, 109–119.e3
30. Yokoyama, M. *et al.* (2014) Inhibition of endothelial p53 improves metabolic abnormalities related to dietary obesity. *Cell Rep.* 7, 1691–1703
31. Chen, Q. *et al.* (2018) Super-resolution tracking of mitochondrial dynamics with an iridium(III) luminophore. *Small* 14, e1802166
32. Miner, G.E. *et al.* (2023) PLIN5 interacts with FATP4 at membrane contact sites to promote lipid droplet-to-mitochondria fatty acid transport. *Dev. Cell* 58, 1250–1265.e6
33. Ouyang, Q. *et al.* (2023) Rab8a as a mitochondrial receptor for lipid droplets in skeletal muscle. *Dev. Cell* 58, 289–305.e6
34. Roberts, M.A. *et al.* (2023) Parallel CRISPR-Cas9 screens identify mechanisms of PLIN2 and lipid droplet regulation. *Dev. Cell* 58, 1782–1800.e10
35. Duan, L. *et al.* (2017) Understanding CRY2 interactions for optical control of intracellular signaling. *Nat. Commun.* 8, 547
36. Jiang, B. *et al.* (2023) Co-condensation with photoexcited cryptochromes facilitates MAC3A to positively control hypocotyl growth in Arabidopsis. *Sci. Adv.* 9, eadh4048
37. Zhang, K. and Cui, B. (2015) Optogenetic control of intracellular signaling pathways. *Trends Biotechnol.* 33, 92–100
38. Mou, X. *et al.* (2023) Organoid models for Chinese herbal medicine studies. *Acta Mater. Med.* 2, 64–71
39. Nguyen, N.T. *et al.* (2021) Nano-optogenetic engineering of CAR T cells for precision immunotherapy with enhanced safety. *Nat. Nanotechnol.* 16, 1424–1434
40. Chen, H. *et al.* (2022) Recent progress in upconversion nanomaterials for emerging optical biological applications. *Adv. Drug Deliv. Rev.* 188, 114414
41. Zheng, B. *et al.* (2017) Near-infrared light triggered upconversion optogenetic nanosystem for cancer therapy. *ACS Nano* 11, 11898–11907
42. Gallardo-Montejano, V.I. *et al.* (2021) Perilipin 5 links mitochondrial uncoupled respiration in brown fat to healthy white fat remodeling and systemic glucose tolerance. *Nat. Commun.* 12, 3320
43. Arvanitis, C.D. *et al.* (2020) The blood-brain barrier and blood-tumour barrier in brain tumours and metastases. *Nat. Rev. Cancer* 20, 26–41
44. Cubillos-Ruiz, A. *et al.* (2021) Engineering living therapeutics with synthetic biology. *Nat. Rev. Drug Discov.* 20, 941–960
45. Lin, Z. *et al.* (2024) Multiscale photocatalytic proximity labeling reveals cell surface neighbors on and between cells. *Science* 385, eadl5763
46. Zhang, Z. *et al.* (2022) Self-assembly of upconversion nanoparticles based materials and their emerging applications. *Small* 18, e2103241
47. Wang, S.W. *et al.* (2022) Current applications and future perspective of CRISPR/Cas9 gene editing in cancer. *Mol. Cancer* 21, 57
48. Liu, Z.L. *et al.* (2023) Angiogenic signaling pathways and anti-angiogenic therapy for cancer. *Signal Transduct. Target. Ther.* 8, 198
49. Yu, S. *et al.* (2019) Advances in nanomedicine for cancer starvation therapy. *Theranostics* 9, 8026–8047
50. Benador, I.Y. *et al.* (2019) Mitochondria bound to lipid droplets: where mitochondrial dynamics regulate lipid storage and utilization. *Cell Metab.* 29, 827–835
51. Lytrivi, M. *et al.* (2020) Recent insights into mechanisms of beta-cell lipo- and glucolipotoxicity in type 2 diabetes. *J. Mol. Biol.* 432, 1514–1534
52. Keenan, S.N. *et al.* (2021) Perilipin 5 S155 phosphorylation by PKA is required for the control of hepatic lipid metabolism and glycemic control. *J. Lipid Res.* 62, 100016

53. Wu, S.C. *et al.* (2022) Stomatin modulates adipogenesis through the ERK pathway and regulates fatty acid uptake and lipid droplet growth. *Nat. Commun.* 13, 4174

54. Xu, G. *et al.* (2024) Mitochondrial ACSS1-K635 acetylation knock-in mice exhibit altered metabolism, cell senescence, and nonalcoholic fatty liver disease. *Sci. Adv.* 10, eadj5942

STAR★METHODS

KEY RESOURCES TABLE

Reagent or resource	Source	Identifier
Bacterial and virus strains		
HBLV-h-PLIN2-mCherry-CRY2-Null-PURO	Hanheng Biotechnology Co., Ltd.	HH20231226GX-LV03
Chemicals, peptides, and recombinant proteins		
Lipi-Blue	Dojindo Laboratories	LD01
MTDR	Thermo Fisher Scientific	#M22426
MTG	Thermo Fisher Scientific	#M46750
FAO-Blue	Funakoshi	#FDV-0033
BODIPY FL C12	Thermo Fisher Scientific	#D3822
Lipi-Red	Dojindo Laboratories	LD03
Etomoxir	Shanghai yuanye Bio-Technology Co., Ltd	S41677
UCNPs	Science Compass Technology Co., Ltd	FMA0826-2
Puromycin Dihydrochloride	Beyotime Biotechnology Co., Ltd.	ST551
Critical commercial assays		
ATP quantitative assay kit	Alicelligent	ALS22032
Annexin V-FITC/PI Apoptosis Kit	ElabElabscience	E-CK-A211
Enhanced Cell Counting Kit 8	Elabscience	#E-CK-A362
Experimental models: cell lines		
Human: 786-O cells	Cell Bank of the Chinese Academy of Sciences	19375.09.3101HUMTCHu186
Human: MCF-7 cells	Cell Bank of the Chinese Academy of Sciences	19375.09.3101HUMSCSP531
Human: HepG2 cells	Cell Bank of the Chinese Academy of Sciences	19375.09.3101HUMSCSP510
Experimental models: organisms/strains		
Mouse: Balb/c	Beijing Weitong Lihua Experimental Animal Technology Co., Ltd	NO.2025051301
Recombinant DNA		
Plasmid: Plin2-mCherry-CRY2	Hanheng Biotechnology Co., Ltd.	HH20230413GX-PC01
Plasmid: Plin2-mCherry	Hanheng Biotechnology Co., Ltd.	HH20230413GX-PC02
Plasmid: Plin2-CRY2	Hanheng Biotechnology Co., Ltd.	HH20230413GX-PC03
Plasmid: Cidec-GFP	Hanheng Biotechnology Co., Ltd.	HH20230413GX-PC04
Other		
U-shaped 96-well plate	Thermo Fisher Scientific	#4515

EXPERIMENTAL MODEL AND SUBJECT DETAILS

Cell culture

786-O and MCF-7 cells (Cell Bank of the Chinese Academy of Sciences) used in this study were cultured in RPMI-1640 medium (11875093, Thermo Fisher Scientific) containing 10% FBS and 100 U/ml penicillin-streptomycin, and HepG2 cells (Chinese Academy of Sciences Cell Bank) were cultured in DMEM (11965092, Thermo Fisher Scientific) supplemented with 10% FBS and 100 U/ml penicillin-streptomycin. All cell cultures in this study were performed in a cell incubator at 5% CO_2 and 37°C. All cell lines used in this study were tested and found to be free of mycoplasma contamination.

Animals

The experimental animals used were 6-week-old healthy female Balb/c nude mice, weighing approximately 18–20 g (Beijing Weitong Lihua Experimental Animal Technology Co., Ltd), with an animal license number of SYXK(LU) 2024 0019. The animal experiment was approved by the Animal Ethics Committee of Shandong First Medical University (2023S 6028). The animal experiment was conducted in accordance with the statutory requirements of the People's Republic of China (GB14925-2010). First, 150 μl of suspension containing cancer cells stably expressing LDLRC (7×10^6 786-O cells per mouse) was subcutaneously injected into the backs of the nude mice. When tumors had formed and grown to approximately 100 mm^3, 150 μg of UCNPs were injected into the tumors, followed by daily 2-h exposure to a 2 W/cm^2 980-nm wavelength NIR LED light (with 20 s of light exposure every 2 min). During the treatment period, the body weight and tumor volume changes of the mice were measured every other day (volume = length × $width^2$ × 0.52). After 15 days of optogenetic therapy, the tumors were dissected, weighed, and photographed. Subsequently, the tumor tissues were embedded, sliced, stained with H&E, imaged (LEICA DM750), and imaged with transmission electron microscopy.

METHOD DETAILS

Engineering LDLRC expression and cell staining

Engineering LDLRC was expressed using the RFect plasmid transfection reagent (21013, Baidai). First, we mixed 3.2 μg of Plin2-mCherry-CRY2, Plin2-mCherry, Plin2-CRY2, or Cidec-GFP (all from Hanbio) with 200 μl of transfection buffer and incubated at room temperature for 5 min to obtain a DNA-transfection buffer mixture. Meanwhile, we mixed 10 μl of RFect with 200 μl of transfection buffer and incubated at room temperature for 5 min to obtain the RFect-Trans buffer mixture. Subsequently, we mixed the DNA-transfection buffer mixture with the RFect-Trans buffer mixture and incubated at room temperature for 15 min to achieve the DNA-RFect-Trans buffer mixture. Finally, we added the DNA-RFect-Trans buffer mixture dropwise into the cell culture medium and cultured it in an incubator for 36 h.

The cells were seeded at a density of 1×10^5 in a 3.5-cm glass-bottomed culture dish containing complete growth medium and incubated in a cell culture incubator for 24 h. Subsequently, the old culture medium was removed, and fresh medium containing 100 nM MTDR (M22426, Thermo Fisher Scientific) or 0.1 μM Lipi-Blue (LD01, Dojindo Laboratories) or 200 nM MTG (M46750, Thermo Fisher Scientific) or 10 μM FAO-Blue (FDV-0033, Funakoshi) was added. The cells were then incubated in the cell culture incubator for 30 min. After staining, the cells were washed three times with preheated PBS at 37°C. Finally, phenol-free medium was added to the cell culture dish, and imaging was performed using confocal (LSM980, Zeiss) or super-resolution microscopy (Lattice SIM, Zeiss).

Live-cell imaging

The live-cell images in this study were acquired using distinct microscopy systems: a 63×/1.4 oil immersion objective on a two-photon confocal microscope (LSM980, Zeiss) and a 63×/1.4 oil immersion objective lens with an ultrahigh-resolution microscope (Elyra 7, Zeiss). The acquired images were analyzed and processed using ZEN software (version 1.1.2.0, Zeiss) and ImageJ software (version 1.52r, National Institutes of Health). The excitation wavelengths and emission detection ranges selected for the fluorescent dyes used in this study were as follows: Lipi-Blue channel: Ex = 405 nm, Em = 417-476 nm; MTDR channel: Ex = 640 nm, Em = 660-700 nm; MTG channel: Ex = 488 nm, Em = 500-550 nm; FAO-Blue channel: Ex = 405 nm, Em = 417-476 nm; C12 channel: Ex = 488 nm, Em = 500-550 nm; LDLRC channel: Ex = 561 nm, Em = 600-640 nm; Lipi-Red channel: Ex = 561 nm, Em = 600-640 nm; Cidec-GFP channel: Ex = 488nm, Em = 500-550 nm.

ATP quantitative analysis and OCR measurement

According to the ATP quantitative assay kit (ALS22032, Alicelligent) manual, the 786-O cells or 786-O expressing LDLRC were seeded at a density of 6000 cells per well in an XFe96 cell culture plate containing complete growth medium overnight. Afterward, 200 μl of XF calibration solution was added to each well of the hydration plate. The probe plate was placed on the hydration plate and incubated for 12 h in a CO_2-free cell culture incubator. Prior to the formal experiment, the cells were subjected to serum starvation or light exposure according to the relevant experiments. Next, the medium in the cell culture plate was replaced with Seahorse detection solution containing 1 mmol/L pyruvate, 2 mmol/L glutamine, and 10 mmol/L glucose, and the cells were incubated in a cell culture incubator without carbon dioxide for 60 min. Following this, 20 μl of 15 μmol/L oligomycin and 22 μl of 10 μmol/L Rot/AA were added to the probe plate. Finally, the probe plate and cell culture plate were transferred to the Seahorse XFe96 instrument (Alicelligent) for ATP quantification analysis and OCR measurement.

FA migration detection

Cells were first incubated in complete medium containing 1.0 μM BODIPY FL C12 (D3822, Thermo Fisher Scientific) for 12 h at 37°C, followed by three washes with prewarmed PBS to remove excess dye. Mitochondria and LDs were then labeled with MTDR and Lipi-Blue, respectively. After serum starvation treatment for the indicated durations, subcellular localization of FAs was determined using super-resolution microscopy (Elyra 7, Zeiss).

Quantification of LD clustering

Using two-photon confocal microscopy to image Lipi-Blue labeled 786-O cell LDs, a total of 728 particles of LDs from 20 cells were obtained from three imaging sessions. The ImageJ software was then used to calculate the average area of the LDs. Based on the average area of the LDs, the degree of LD clustering was classified as either nonclustered or clustered.

Light source construction

Blue light source used in cell experiments consisted of six blue LEDs emitting a wavelength of 450 nm (1 W) connected in parallel on a circuit board, with a diffuser placed on top and connected to an adjustable constant voltage power supply. The power supply was adjusted to maintain a constant blue light optical power of 500 μW/cm^2 on the outer surface of the diffuser. The applied blue light power has been demonstrated in relevant studies to exhibit low phototoxicity to cells [37]. During blue light exposure, the cell culture dishes were placed on the light diffuser plate inside the incubator for exposure according to the experimentally designated durations.

NIR light source used in animal experiments employed LED lights emitting NIR light at a wavelength of 980 nm (50 W) with an exposure angle of 90°. The constant voltage power supply was adjusted to ensure that the optical power of NIR light on the outer surface of the light source remained constant at 2 W/cm^2. The NIR light optical power used in this study has been confirmed as effective in relevant research [39].

Cell scratch and proliferation assay

786-O cells expressing LDLRC (Plin2-mCherry-CRY2) or LDLRC-c (Plin2-mCherry) were cultured in 6-cm cell culture dishes until 100% confluence was reached. They were then serum-starved for 2 h while being illuminated for 0, 1, and 2 h. Next, a blank line was drawn across the cell layer using a 200-μl pipette tip. After that, the healing of the scratch was observed at 0 and 12 h postculture using a confocal microscope (EVOS M7000, Thermo Fisher Scientific) with a 20× objective lens.

786-O cells expressing LDLRC (Plin2-mCherry-CRY2) or LDLRC-c (Plin2-mCherry) were exposed to serum starvation for 2 h while simultaneously being exposed to light for 0, 1, or 2 h. Subsequently, 8000 cells were seeded into each well of a 96-well plate and cultured overnight. The detection was then carried out following the experimental instructions of CCK8 (E-CK-A362, Elabscience).

Efficacy assessment at the cellular spheroid level

786-O cells expressing LDLRC (Plin2-mCherry-CRY2) or LDLRC-c (Plin2-mCherry) were seeded in a U-shaped 96-well plate (4515, Thermo Fisher Scientific) at a density of 1 × 10^4 cells per well and incubated until tumor spheroids formed. The tumor spheroids were then exposed to light for 0, 1, and 2 h, and after 12 h, the spheroids were observed and imaged using a confocal microscope (EVOS M7000, Thermo Fisher Scientific) with a 20× objective lens.

Lentiviral transfection and resistance screening

786-O cells were seeded at a density of 2 × 10^5 cells per well in a 6-well plate. When the cell confluence reached 50%, the old culture medium was removed and replaced with 1 ml of fresh culture medium containing 20 μl of lentiviral solution (all from Hanbio) (stable expression of Plin2-mCherry-CRY2 lentivirus, and the infective multiplicity of infection value has been determined through preliminary experiments). After 4 h, an additional 1 ml of culture medium was added, and the medium was replaced 24 h later. The infection efficiency was observed using confocal microscopy 48 h postinfection. After infection, the culture medium was changed to fresh medium containing 1 μg/ml puromycin. After 24 h, the fresh culture medium was replaced, and the cells were cultured for an additional 24 h. Then, confocal microscopy was used to observe and record the fluorescence signal of Plin2-mCherry-CRY2.

QUANTIFICATION AND STATISTICAL ANALYSIS

The data calculation and analysis were performed using Origin (Origin, 2021) and Excel (Microsoft, 2013). A two-tailed unpaired Student's *t* test was used for statistical analysis, and the data were expressed as mean ± SEM. Statistical significance was considered when $P < 0.05$. Colocalization analysis, LD number/area quantification, LD–mitochondria contact quantification, and fluorescence intensity measurements were conducted using ImageJ software. All figures were created using PowerPoint (Microsoft, 2013) and BioRender.com. Statistical significance and sample sizes for all graphs were indicated in the respective figures and figure legends.

Document S1, containing supplemental Figures S1–S17.